Picosecond charge transport in rutile at high carrier densities studied by transient terahertz spectroscopy

V. Zajac,[1,2] H. Němec,[1] and P. Kužel[1]

[1]*Institute of Physics, Academy of Sciences of the Czech Republic, Na Slovance 2, 182 21 Prague 8, Czech Republic*

[2]*Institute of Applied Physics and Mathematics, Faculty of Chemical Technology, University of Pardubice,*
Studentská 95, 532 10 Pardubice, Czech Republic

We study terahertz photoconductivity of a rutile single crystal between 10 and 300 K under strong photoexcitation by femtosecond pulses at 266 nm. A marked dependence of the carrier mobility on the carrier density is observed leading to highly complex transport phenomena on a picosecond time scale. We develop a general model of carrier photoconductive response in the case of time dependent inhomogeneous distribution of carrier density and mobility. This allows us to assess an important role of both electrons and holes in the response of photoexcited rutile. At low temperatures, the carrier mobility is initially reduced due to the electron-hole scattering and increases by one order of magnitude upon ambipolar diffusion of the carriers into deeper regions of the sample. At room temperature, contributions of transient hot optical phonons and/or of midinfrared polaron excitations with charge-density-dependent dielectric strength emerge in the photoconductivity spectra.

I. INTRODUCTION

Titanium dioxide is an important material finding an extremely broad range of applications. Unlike most classic semiconductors, the rutile form of TiO_2 is characterized by a very strong electron-phonon coupling which is responsible for the very low carrier mobility [1]. Although titanium dioxide nanoparticles are widely used as the electron conductor, e.g., in Grätzel cells [2], charge transport in titanium dioxide is still a subject of scientific debates both in its bulk [3,4] and nanocrystalline forms [5,6].

Optical pump-terahertz probe (OPTP) spectroscopy is a convenient tool for determining transport properties of charge carriers in bulk, thin film, and nanostructured semiconductors without the need of attaching electrical contacts to the sample. It measures the temporal wave form of the electric field E of a probing THz pulse transmitted through a sample in unexcited state (reference measurement) and the change of the transmitted field ΔE upon photoexcitation. Thanks to the detection of the field in the time domain, the Fourier transformation yields both the amplitude and phase of the transient transmittance, which subsequently provide the real and the imaginary part of the spectral response of photoexcited charge carriers without Kramers-Kronig analysis.

The aim of this work is to characterize the response function of mobile carriers in (001)-oriented bulk rutile, i.e., to determine their THz dynamic mobility $\mu(\omega)$ in the ab plane with emphasis on their behavior at high carrier densities. We study in detail the response of carrier populations with an inhomogeneous depth distribution. Compared to previously published investigations [4] we include in our study the process of carrier diffusion through a high photocarrier density gradient and through detecting the carrier response in time. We develop a general theoretical description of the carrier response involving spatially inhomogeneous carrier density and mobility distributions in the sample and their time evolutions. The model is then applied to data measured at various pump-probe delays and with various excitation densities. This provides an in-depth picture of the carrier transport in rutile. Measurements at high temperatures reveal a tail of midinfrared polaron excitations.

II. THEORETICAL DESCRIPTION

It is expected that, in a bulk homogeneous semiconductor, the dynamic mobility of charges (or more precisely, of the corresponding electron and hole polarons in the case of TiO_2) follows the Drude formula:

$$\mu_i(\omega) = \frac{e\,\tau_i}{m_i^*} \frac{1}{1 - i\omega\tau_i}, \quad i = e,h, \tag{1}$$

where e stands for elementary charge and τ_i is the momentum scattering time of the charge carrier (index i is e for electrons and h for holes). In rutile the charge carrier mass is increased due to the formation of the polaron [3] and, consequently, the polaron effective mass m_i^* is introduced in (1).

For bulk samples with a thin photoexcited layer, the measured transient transmittance $\Delta E/E$ in the frequency domain is directly related to the transient sheet conductivity $\Delta\Sigma$ as follows [7–9]:

$$-\frac{1}{e\phi} \frac{1 + n(\omega)}{z_0} \frac{\Delta E(\omega)}{E(\omega)} = \frac{\Delta\Sigma(\omega)}{e\phi} = \xi\mu^{\mathrm{avg}}(\omega), \tag{2}$$

where ϕ is the excitation photon fluence entering the sample, n is the complex refractive index of the unexcited sample in the THz range, and z_0 is the vacuum wave impedance (this expression is valid in the small signal limit, $\Delta E/E \ll 1$). In many semiconductors, the response of carriers of only one type dominate in the photoconductivity and their mobility is independent of their position (depth) in the sample. The middle term in (2), expressing the normalized transient sheet conductivity, then transforms to a simple product of the carrier mobility $\mu^{\mathrm{avg}} \equiv \mu$ and of the carrier photoexcitation quantum yield ξ. In a good quality single crystal there is no *a priori* reason to consider ξ significantly different from 1 immediately after photoexcitation; Eq. (2) then provides a direct relationship between the measurable signal and the carrier mobility.

In more complex systems (including multiple types of carriers or depth-dependent mobility μ), a single mobility and quantum yield become meaningless; the right-hand side of (2) can be interpreted as the mobility averaged over all (initially) photoexcited carriers and it is practical to set $\xi = 1$.

For a strong absorption of the pump pulse, a very inhomogeneous population of free carriers is achieved with a high carrier density close to the surface and an order of magnitude lower carrier density just a few tens of nanometers below the photoexcited surface. Moreover, such a steep carrier density profile is expected to vary quite significantly in time due to diffusion and recombination of carriers. The electron-hole scattering and the carrier scattering on phonons may become important in good quality semiconductors. Hendry *et al.* [4] reported that at high excitation densities the Drude scattering time in rutile depends on the excitation fluence. It then directly follows that the carriers at different depths must exhibit different mobilities. Below we develop a theoretical framework to understand the exact meaning of the averaged mobility μ^{avg} in this situation.

We deal with a homogeneous single crystal sample with a very thin photoexcited surface layer (the penetration depth of the pump beam is $\sim$12 nm [10]) with carrier density depth-profile $N_i(z)$. The transient sheet conductivity in (2) then involves integration of the local transient conductivity $e\mu_i N_i$ over the sample thickness L and one obtains

$$\mu^{\text{avg}}(\omega,t) = \frac{1}{\phi} \sum_{i=e,h} \int_0^L \mu_i[\omega; N_i(z,t)] \, N_i(z,t) \, dz. \quad (3)$$

The time t in (3) describes the transient dynamics of the sample, i.e., in the experiment it is the time delay between the optical pump and THz probe pulses. The carrier mobility depends on time and on depth implicitly, through its dependence on the carrier density N_i. Note that with this definition the decay of the carrier density is also formally involved in the time dependence of $\mu^{\text{avg}}(\omega,t)$. In the case of a weak excitation, μ is almost independent of N and one trivially finds the interpretation: $\mu^{\text{avg}}(\omega,t) = \mu_e(\omega)\xi_e(t) + \mu_h(\omega)\xi_h(t)$. The parameters $\xi_i(t)$ represent here the ratio between the number of free electrons/holes in the sample at time t and the number of excitation photons per pulse, i.e., they describe the carrier number decay

$$\xi_i(t) = \frac{1}{\phi} \int_0^L N_i(z,t) \, dz. \quad (4)$$

The value of $\xi_i(0)$ defines the initial quantum yield, which in our good quality sample is assumed to be 1 as mentioned above. At high carrier concentrations, the dependencies $\mu_i(\omega; N_i)$ and $N_i(z,t)$ must be found to evaluate the integral in (3).

Hendry *et al.* [4] proposed two mechanisms to be responsible for a change of the carrier mobility with the carrier density: carrier-carrier scattering, and scattering of carriers on acoustic phonons. In this view the carrier mobility (1) is controlled by the density dependent value of the momentum scattering time:

$$\frac{1}{\tau_i(N_i)} = \frac{1}{\tau_{0i}} + aN_i + b_i(N_i)^{1/3}, \quad (5)$$

where τ_{0i} stands for the scattering time in the low-density limit, the second right-hand-side term describes the electron-hole

scattering process, which may substantially contribute to a reduced photocurrent at high photocarrier densities, and the last term reflects an enhanced scattering of carriers on acoustic phonons. This is related to an increase of the carrier Fermi velocity $\propto N^{1/3}$ due to the band filling at high carrier densities. Since the carrier mean free path between collisions on acoustic phonons is constant at a given temperature T [11], the constants b_i can be estimated from parameters of carrier transport at low densities (cf. Eq. (2) and footnote 24 in [4]).

The optical excitation pulse is shorter than 50 fs in our setup, therefore we can assume that the carriers are generated instantaneously at time $t = 0$. Their initial density profile in the sample is exponential owing to the Lambert-Beer absorption law:

$$N_i(z,0) = \alpha\phi \, \exp(-\alpha z), \quad (6)$$

where α is the optical absorption coefficient of the sample at the wavelength of the pump pulse. On a longer time scale the carrier density depth profile $N_i(z)$ may be strongly influenced by diffusion and recombination of carriers. The space-time evolution of the carrier density is then given by a pair of diffusion equations for electrons and holes:

$$\frac{\partial N_i(z,t)}{\partial t} = D_A \frac{\partial^2 N_i(z,t)}{\partial z^2} - B \, N_e(z,t)N_h(z,t),$$
$$i = e,h, \quad (7)$$

with the initial conditions given by (6). The last right-hand-side term describes bimolecular carrier recombination with a rate constant B. There are no signatures of carrier trapping at investigated times ($\leqslant$600 ps) after photogeneration. D_A is the ambipolar diffusion coefficient

$$D_A = \frac{D_e\mu_h + D_h\mu_e}{\mu_e + \mu_h}, \quad (8)$$

which forces diffusion of both electrons and holes to occur with the same rate because the electrostatic interaction between them prevents the more mobile carrier type from diffusing away from the less mobile one. It follows that densities remain the same for electrons and holes: $N(t,z) \equiv N_e(t,z) = N_h(t,z), t \leqslant 600$ ps. Similar diffusion equations have been solved in the case of ultrafast carrier dynamics in ion irradiated InP [12] and $In_{0.53}Ga_{0.47}As$ [13] in order to take into account the carrier diffusion on the time scale of tens to hundreds of picosecond.

Diffusion coefficients of electrons and holes are connected to their dc mobilities through the Einstein equation

$$D_{e,h} = \frac{\mu_{e,h}k_B T}{e}, \quad (9)$$

where T is temperature and k_B is the Boltzmann constant. Thus, to develop a completely consistent model, we need to consider that the diffusion coefficient in (7) depends on the density of carriers through the scattering times as defined by (5). The coefficient a describing the electron-hole scattering in (5) must be the same for both types of charge carriers. On the other hand, the scattering on acoustic phonons described by the coefficients b_i may in principle differ for electrons and holes,

due to their different masses, and we can write

$$\frac{1}{D_A(N)} = \frac{1}{2k_BT}\left[\left(\frac{m_e^*}{\tau_{0e}} + \frac{m_h^*}{\tau_{0h}}\right) + a(m_e^* + m_h^*)N \right.$$
$$\left. + (b_e m_e^* + b_h m_h^*)N^{1/3}\right], \quad (10)$$

where N is the density of either carrier type.

This defines our plasma diffusion model. A numerical solution of the system of diffusion equations (7) with the diffusion coefficient (10) permits evaluation of the integral (3) where the mobilities μ_i defined by (1) depend on N through momentum scattering times τ_i following (5). The integrated mobility spectra evaluated at given probing times t with given excitation fluences ϕ can then be compared to a set of experimental spectra measured at corresponding pump-probe delays and fluences. The input parameters (carrier effective masses m_i^*, low-density scattering times τ_{0i}, electron-hole scattering rate a, carrier-phonon scattering rates b_i, and bimolecular recombination rate B) are then iteratively changed to obtain the best global fit of all experimental spectra at the same time.

The averaged mobility μ^{avg} defined by (2) is considered as an experimental spectrum in this paper and reflects both the evolution of the mobility spectra and the carrier density decay. It is analogous to the normalized transmission function ΔT_{norm} introduced in [9,14]: these two quantities differ just by a multiplication factor,

$$\Delta T_{norm} = \frac{2}{1+n}\mu^{avg}. \quad (11)$$

III. EXPERIMENT

The experiments were performed in a usual setup for the optical pump-THz probe spectroscopy driven by a Ti:sapphire femtosecond laser amplifier (Spitfire ACE, central wavelength 800 nm, 1 mJ pulse energy, 5 kHz repetition rate, <50 fs pulse length) [15]. One part of the laser beam was used for the generation of probing THz pulses using optical rectification in a 1 mm thick (110)-oriented ZnTe crystal. Another part of the laser beam was used for detection of the THz pulses through electro-optic sampling in another ZnTe crystal. The whole THz part of the experiment was enclosed in a box allowing us to achieve primary vacuum in order to avoid THz absorption on water vapor.

The third part of the laser beam was frequency tripled to 266 nm (4.66 eV) and defocused to generate photocarriers homogeneously across the sample surface (less than 28% of the pump beam power was transmitted through a 3 mm aperture serving as the sample holder). The photon fluence ϕ_{inc} incident on the sample front surface was varied by using an UV polarizing attenuator and carefully determined: the excitation photon fluence was calculated as $\phi = \phi_{inc}(1 - R)$ and its values ranged from 2×10^{13} to 2.5×10^{14} photons/cm^2 at room temperature and from 2×10^{12} to 1.6×10^{14} photons/cm^2 with the cryostat; the initial photocarrier density at the sample surface then equals $N = \alpha\phi$ ($\alpha = 85$ μm^{-1}; $R = 0.354$ is the sample front surface optical reflectance at 266 nm [10]).

The sample, a 0.26 mm thick 10×6 mm^2 large c-cut rutile single crystal, was placed in an optical cryostat (Oxford, Optistat) with a pair of sapphire input windows (transparent
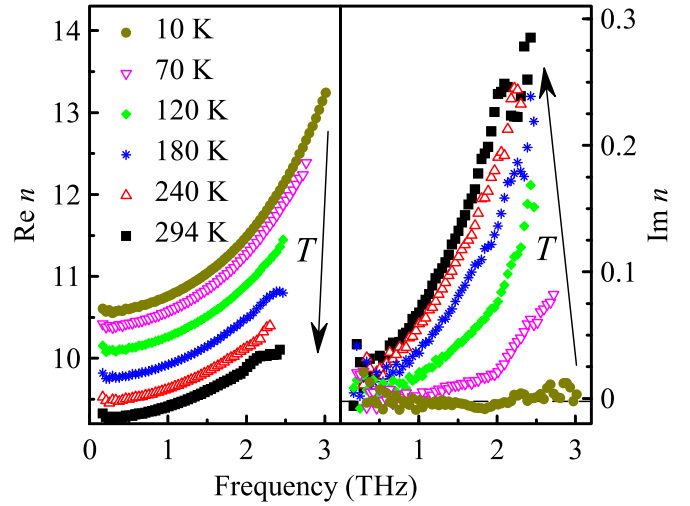

FIG. 1. Real and imaginary part of measured complex refractive index of rutile without photoexcitation (electric field perpendicular to the c axis).

for both optical pump and THz probe pulses) and a pair of thin Mylar output windows (transparent for THz probe pulses). Room temperature measurements were carried out without the cryostat. The transient THz conductivity spectra were measured at temperatures of 10, 70, 180, and 300 K under various excitation fluences and at several pump-probe delays. The measurements of the transient spectra at the lowest excitation densities took about 2 h at 10 K and more than 15 h at room temperature.

Alternatively, pump-probe scans (transient dynamics) were also measured: the negative maximum of the transient THz wave form ΔE_{max} was found for the pump-probe delay $t = 10$ ps and, subsequently, the pump-probe delay scan was performed for this position on the wave form. The maximum amplitude of the reference wave form E_{max} (with the pump beam off) served for the signal normalization.

IV. RESULTS AND DISCUSSION

The complex equilibrium refractive index n of the sample in the THz range was first measured (see Fig. 1) in order to allow calculation of μ^{avg} from the raw experimental data $\Delta E/E$ using Eq. (2). At higher temperatures we observe a dispersion and an absorption tail of the lowest-frequency polar phonon at 183 cm^{-1} [16]; the phonon damping progressively decreases as the temperature is lowered.

In Fig. 2 we plot examples of transient wave forms used for evaluation of μ^{avg} spectra. The ringing in the reference wave form measured at 10 K is due to a chirp induced upon the pulse propagation in the dispersive sample; the oscillations are attenuated at higher temperatures due to a stronger absorption (cf. Fig. 1). The phase shift of the room temperature transient wave form is π which means that the real part of the conductivity dominates (i.e., the conduction band electrons cause mainly absorption of the THz wave and their momentum scattering time is short). In contrast, the wave form at 10 K exhibits a phase shift between $2\pi/3$ and $\pi/2$; this is related to a significant imaginary part of the photoconductivity (dispersion, long momentum scattering time).
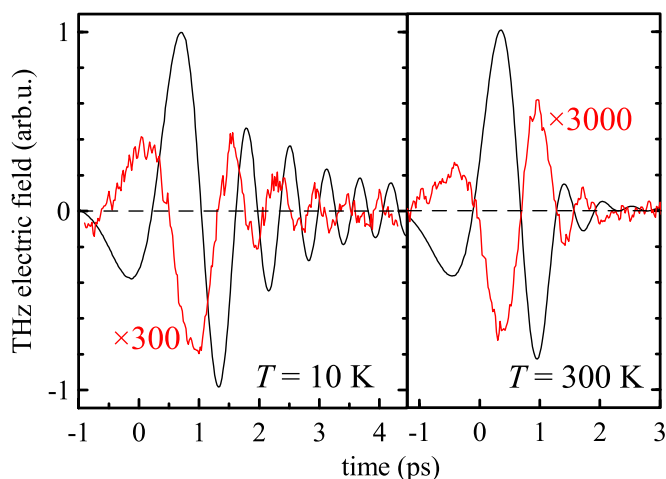
FIG. 2. Examples of measured wave forms. Black lines: reference wave forms (pump beam off), red lines: transient wave forms (magnified). $T = 10\,\text{K} : \phi = 6 \times 10^{12}$ photons/cm^2, $t = 11$ ps, 25 min data accumulation; $T = 300\,\text{K} : \phi = 2 \times 10^{13}$ photons/cm^2, $t = 10$ ps, 15 h data accumulation.

A. Transport at low temperatures

The transient dynamics were measured at 10 and 70 K at the highest excitation fluence available with cryostat (see Fig. 3). We observe a nanosecond decay preceded by an unusually long build-up of the transient response on a hundred picosecond time scale. Our hypothesis is that this behavior is related to a low initial mobility of carriers due to their high concentration in agreement with (5). At longer pump-probe delays, the density of carriers is reduced due to their diffusion and recombination. We thus observe a competition between the transient conductivity growth and decay due to an increase of the carrier mobility and a decrease of the free carrier number, respectively. This effect is much more pronounced
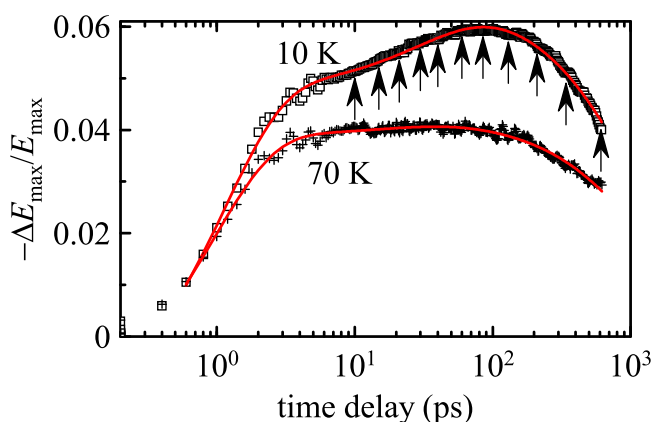

FIG. 3. Transient dynamics in rutile excited with fluence $\phi = 1.6 \times 10^{14}$ photons/cm^2. Symbols: Measured dynamics of transient THz response at 10 K (squares) and 70 K (crosses). The lines serve as guides to the eye. The arrows indicate time delays corresponding to transient spectra investigated at the highest excitation density within the general plasma diffusion model. Note that the horizontal axis is shifted in order to include the time of the excitation event (at 1 ps in the plot).
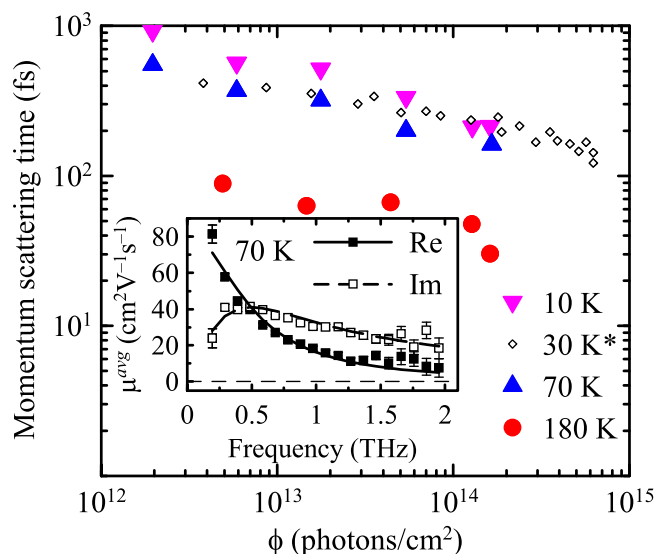

FIG. 4. Momentum scattering times obtained by fits of individual transient spectra with the single-component Drude model. Spectra were measured 9–11 ps after photoexcitation. *The data at 30 K are taken from [4]. Inset: (symbols) THz mobility spectrum at 70 K, $t = 10$ ps, at a moderate excitation fluence (1.8×10^{13} cm^{-2}); (lines) a fit with the single-component Drude formula.

at 10 K: the signal rises by 20% between 6 and 100 ps; at 70 K nearly a flat curve is observed between 6 and 100 ps (Fig. 3). We will analyze the measured spectra and dynamics on two different levels. First we use a *single-component Drude model* for fitting of individual spectra of μ^{avg} at various temperatures and excitation fluences; this allows us to compare our data directly with previous works. Subsequently, we apply a *general plasma-diffusion model* to perform a global fit of a set of 23 spectra of μ^{avg} at 10 K (data measured at various pump-probe delays and at various excitation fluences). This approach allows us to draw quantitative conclusions on electron and hole transport.

1. Single-component Drude model

The spectra μ^{avg} were first fitted directly with the simple Drude model (1) assuming one dominant carrier type with the purpose to compare our fluence-dependent experimental data to those obtained by Hendry *et al.* [4]. The momentum scattering times retrieved from these fits for various temperatures and excitation fluences obtained at a short time after photoexcitation are shown in Fig. 4. An example of the spectrum and of the fit for a low excitation fluence at 70 K is displayed as an inset of this figure. A very good correspondence between our results and those published in [4] is found indicating that samples with very similar quality were used in these two studies. As shown in [4], the observed increase of the scattering rate with increasing excitation fluence is consistent with (5). The carrier transport parameters of [4] are shown in the first row of Table I. A decrease of the scattering time with increasing temperature, also clearly seen in Fig. 4, quantitatively agrees with the previous study of polaron motion in rutile [3]. As pointed out above, evolution of the response of carrier population in time is quite complex and

TABLE I. Coefficients characterizing the carrier transport and decay as obtained from transient THz measurements. Indices Lt and Hv denote, respectively, the lighter and heavier of the electron and hole polarons. In [4] (first row of the table) electrons were considered as a much more mobile carrier type. Our results—global fits of the measured mobility spectra (with variable pump-probe delay and excitation fluence)—are shown in rows 2 and 3. The parameters in the second row were obtained from our data under an additional assumption of the same properties of electron and hole polarons. Note that b is negligible for both electrons and holes in our fits. The error values are standard deviations provided by the fit.

	$m_{Lt}^*(m_0)$	$m_{Hv}^*(m_0)$	τ_{0Lt} (fs)	τ_{0Hv} (fs)	$a(10^{-20}$ cm^3/ps)	$b_{e,h}(10^3$ m/s)	$B(10^{-23}$ cm^3/ps)
From [4]	6	–	~600	–	0–2.3	$b_e = 4$–8	–
$\mu_e = \mu_h$	10.8 ± 0.1		690 ± 20		6.1 ± 0.3	0 ± 0.01	6.1 ± 0.4
$\mu_e \neq \mu_h$	7.5 ± 0.5	12 ± 1	280 ± 20	$\gtrsim 10$ ps	6.7 ± 0.2	0 ± 2	6.3 ± 0.3

an attempt to perform simple Drude fits of spectra measured at longer pump-probe delays (such spectra were not measured in [4]) leads to a complicated behavior of the parameters and does not provide a deeper insight into the processes in rutile. In order to interpret these experimental spectra, a more complex model is considered below.

2. General plasma diffusion model

We start from the hypothesis of a competition between two processes: increase of the mobility of inhomogeneously distributed carriers due to the diffusion on the one hand, and decrease of the carrier number due to their recombination on the other hand. In order to check semiquantitatively, that it is a very pertinent hypothesis, we first set up a *two-component Drude model* describing a coexistence of a dense and a less dense plasma in the sample. This model provides a very useful insight into the observed carrier dynamics and fitting of the spectra with this still relatively simple model provides clear justification of the proposed picture of the carrier transport. This model is presented in the Supplemental Material (Sec. 1) [17].

Quantitative conclusions on the carrier transport are obtained from the general plasma diffusion model introduced in the theoretical section above. It was applied to the data measured at 10 K where effects of the diffusion are most pronounced: eleven spectra measured at the maximum fluence

of 1.6×10^{14} photons/cm^2 for pump-probe delays between 9 and 600 ps indicated by arrows in Fig. 3; eight spectra measured at a lower fluence of 1.3×10^{14} photons/cm^2 between 11 and 600 ps; four spectra at $t = 10$ ps at further decreased fluences of 5.4×10^{13}, 1.8×10^{13}, 5.9×10^{12}, and 2.0×10^{12} photons/cm^2.

This ensemble of 23 complex transient THz spectra $\mu^{avg}(\omega)$ was fitted over the frequency interval 0.19–1.9 THz with a single set of eight fitting parameters which define the model. The model is quite complicated and the influence of individual parameters on the mobility spectra is not straightforward; also, correlations between some parameters may be *a priori* expected. For this reason, we present a deeper technical discussion of the fitting in the Supplemental Material [17]. Several examples of experimental spectra and their fits are shown in Fig. 5. The converged parameters of the fits are summarized in Table I.

3. Analysis

The signal measured by transient THz spectroscopy reflects the total photoconductivity of the sample. In this study, based on the detailed analysis of the carrier diffusion and scattering in the high and low carrier density regimes, we aim to disentangle the contribution of electrons and holes. However, THz spectroscopy cannot specifically discriminate between the photocurrents generated by positive and negative
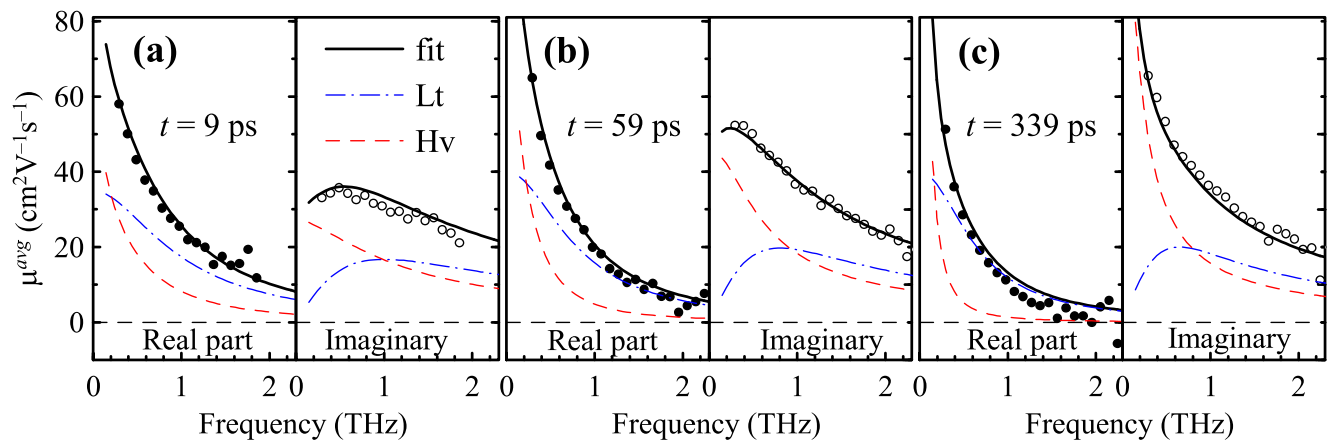

FIG. 5. Transient THz spectra $\mu^{avg}(\omega)$ at 10 K at selected pump-probe delays t (indicated) at the highest fluence $\phi = 1.6 \times 10^{14}$ photons/cm^2. Symbols: Experimental data. Full black lines: Global fit with the general plasma diffusion model and its decomposition into contributions of electron and hole polarons (blue dash-and-dot lines: contribution of the lighter of the two polarons; red dashed lines: contribution of the heavier polaron).

charge carriers; the fits of the data allow us to distinguish only between the contributions of lighter and heavier carriers (polarons) of the two types. Concerning the attribution of effective masses to electron and hole polarons in rutile the currently available data do not provide an unambiguous answer. In some older works it has been argued that the effective mass of holes is much smaller than the effective mass of electrons ($m_h^* < m_0$, $m_e^* \gg m_0$) [18,19], where m_0 is the electron rest mass. Later on, it was shown by transient diffraction grating experiments [20] that the effective mass of the hole polarons in TiO_2 single crystals is $m_h^* > 3m_0$. The value of effective mass of electron polarons was then frequently reported to be in the range of $m_e^* \approx (5\text{–}13)m_0$ as summarized in [21,22]. It is also interesting to note that the effective electron mass as inferred from experiments seems to be larger than the effective hole mass in the anatase form of TiO_2 [21,22]. Recent first-principle calculations within the local density approximation [23] and taking into account various corrections [24] determine the band structure of rutile and predict the band mass of electrons and holes and their anisotropy. The Fröhlich electron-phonon coupling theory then provides the electron and hole polaron effective masses in the *ab* plane of $2.4m_0$ and $8m_0$, respectively [24], i.e., the hole polaron being heavier. Previously, Glassford and Chelikowsky [25] found very similar masses of the charge carriers in rutile; however, a follow-up study, carried out by Hendry *et al.* [3] within the Feynman polaron theory, determines the electron polaron mass in the *ab* plane to be as high as $15m_0$.

The large scatter of the literature values of polaron effective masses may be caused by the variable quality of the crystals or films used in various experiments (namely oxygen vacancies in TiO_2 may strongly influence the polarization of the lattice and, consequently, alter the electron-phonon coupling leading to the polaron effect), by the anisotropic character of the compound and by the complexity of the carrier-phonon system. Our findings below confirm that polarons of both polarities significantly contribute to the measured transient THz spectra and to their evolution in time. As, based on the available literature, we are not able to attribute unambiguously the lighter of the two polarons to electrons or holes, we will rather refer, in the following discussion, to the "lighter" polaron (index Lt) and the "heavier" polaron (index Hv) instead of hole and electron polarons. We always keep in mind that these two polarons are related to opposite charges.

In some fits we assumed that the electron and hole polarons possess very similar properties. In this case effective masses and scattering times were set equal in the fitting procedure. This fit allows us to decrease the number of independent fitting parameters to 5. Based on all our fits (see Supplemental Material for further details on all examined variants of the fit [17]), we can draw the following partial conclusions.

(i) Our data are clearly *not* compatible with the assumption $\mu_{Lt} \gg \mu_{Hv}$ (where $m_{Lt}^* \ll m_{Hv}^*$) and the contribution of both electrons and holes to the photoconductivity is significant. On the other hand, the data are compatible with the assumption $\mu_{Lt} \approx \mu_{Hv}$; more precisely, the fits indicate that the masses of the two polarons are in the range of 7–13 with the lighter polaron tending to the lower part of this range and the heavier polaron being in its upper part.
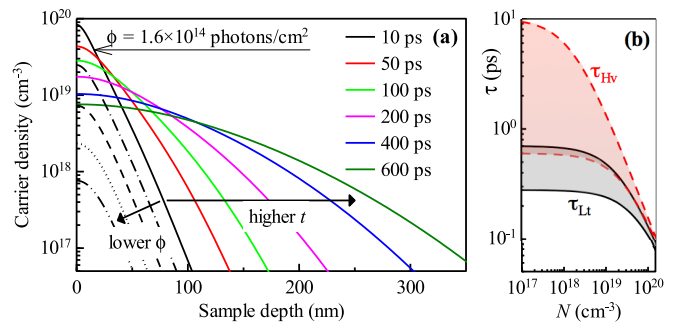

FIG. 6. (a) Calculated carrier density profiles inside the sample for selected pump-probe delays and fluences; colored lines: excitation fluence of 1.6×10^{14} photons/cm^2, the pump-probe delay is increased along the arrow (values are provided in the legend); black lines: pump-probe delay 10 ps, the excitation fluence is decreased along the arrow (values: 5.4×10^{13}, 1.8×10^{13}, 5.9×10^{12}, 2.0×10^{12} photons/cm^2). (b) Carrier density dependence of the momentum scattering time estimated from (5) and values in Table I.

(ii) The dominant scattering mechanism at high photocarrier densities is electron-hole scattering ($a \approx 6 \times 10^{-20}$ cm^3/ps). The carrier-phonon scattering is not observed in our sample at 10 K and can make a significant contribution only in doped samples with a single type of carriers where the carrier-carrier scattering does not influence the charge transport.

(iii) The bimolecular recombination coefficient is $B \approx 6 \times 10^{-23}$ cm^3/ps.

(iv) The lighter polaron tends to have about one order of magnitude shorter scattering time than the heavier one. This implies that the dc conductivity is carried rather by the heavier polarons as also observed in Fig. 5 where the signal decomposition into contributions of lighter and heavier polarons is shown [contribution of heavier polarons to $\mu^{avg}(\omega)$ dominates at low frequencies]. The low-density mobility of the lighter polaron at 10 K is estimated to be 60–120 cm^2 V^{-1} s^{-1}. However, this last conclusion must be taken with caution as the fit probably underestimates the low-density scattering rate of the heavier polaron (the fit is insensitive to the value of τ_{0Hv} when it rises above several picoseconds).

Figure 6(a) shows the time evolution of the calculated carrier density profile at the highest excitation fluence corresponding to the best fit with the general plasma-diffusion model. The carrier density at the surface decreases by an order of magnitude during the initial 600 ps and the spatial width of the density distribution substantially broadens. In Fig. 6(b) we plot the dependence of the calculated momentum scattering times on the carrier density as it results from the fits.

B. Transient phonon response at room temperature

At room temperature the averaged mobility $\mu^{avg}(\omega)$ drops to 2 cm^2 V^{-1} s^{-1}, cf. Fig. 7(a). Such a weak response made it impossible to decrease the excitation fluence as low as in measurements at cryogenic temperatures. We observe that upon increasing the excitation density [Figs. 7(a)–7(c)] the real part exhibits a small decrease of its value. This is consistent with the density dependent electron-hole scattering (5) observed at cryogenic temperatures. However, the slope of the imaginary
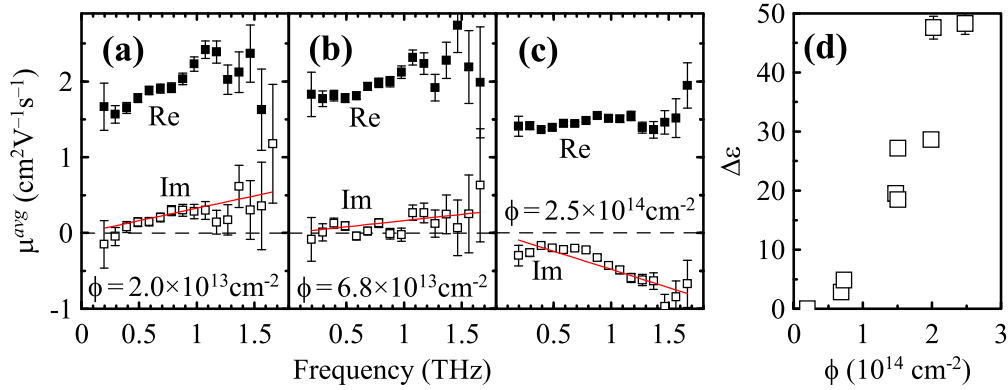
FIG. 7. Room temperature transient THz spectra $\mu^{\text{avg}}(\omega)$ at (a) low, (b) medium, and (c) maximum excitation fluences (indicated in the plots) at 266 nm, measured 10 ps after photoexcitation. Symbols: data, full red lines: linear fit of Im[$\mu^{\text{avg}}(\omega)$] with (12). (d) Positive contribution to the permittivity related to the slope change of the mobility spectra versus excitation fluence.

part of $\mu^{\text{avg}}(\omega)$ flips gradually from positive to negative values. The increased scattering rate of free carriers by itself (5) may only lead to a decrease of the imaginary part of the mobility (1) to lower positive values. This indicates that on top of the carrier conductivity, an additional response emerges due to some other kind of bound polar excitations, which are sensitive to the pump fluence. Such an observation is enabled namely by the fact that carriers in TiO$_2$ exhibit such an extremely low mobility at high temperatures, and the additional localized response in the spectrum is thus not hidden in their Drude conductivity peak.

The observed approximately linear slope of the imaginary part of $\mu^{\text{avg}}(\omega)$ corresponds to a constant contribution to the transient real permittivity $\Delta\varepsilon$ that was determined by a linear fit [red solid lines in Figs. 7(a)–7(c)]

$$\text{Im}[\mu^{\text{avg}}(\omega)] = -\varepsilon_0(\Delta\varepsilon_{\text{Drude}} + \Delta\varepsilon)\frac{\omega}{e\alpha\phi} \qquad (12)$$

of nine spectra measured at different pump fluences. We assume that at the lowest available charge carrier density, any additional localized response can be neglected ($\Delta\varepsilon = 0$) and the initial positive slope of ~ 0.3 cm^2 V^{-1} s^{-1} per 1 THz [Fig. 7(a)] at the lowest available charge carrier density corresponds solely to the Drude response of mobile polarons with an average scattering time of about 20–30 fs ($\Delta\varepsilon_{\text{Drude}} \approx -1.6$). We observe in Fig. 7(d) that $\Delta\varepsilon$ makes a substantial contribution to equilibrium properties (cf. Fig. 1) at high photocarrier densities. Below we propose several phenomena that we find relevant to the observed dependence of the dielectric strength: effects of hot phonon modes and polaron-polaron interaction.

The pump photon energy of 4.7 eV exceeds the carrier band gap by 1.5 eV; this excess energy of photocarriers is rapidly transferred to the lattice, i.e., a nonequilibrium population of optical and acoustic phonons is generated in the excited layer of the sample. The equilibrium parameters (eigenfrequency Ω and oscillator strength) of certain phonon modes can be altered under these conditions due to their anharmonic character. Pashkin *et al.* [26] directly observed characteristic spectral signatures of hot polar phonon population induced by optical pumping of a high-temperature superconductor in the frequency range above 8 THz. Here we are probing at much lower frequencies, which means that we sense a transient change of

the *static* permittivity of some high-frequency phonon modes. The related spectral changes in the real THz permittivity (or imaginary conductivity) are predominantly due to the change of the phonon eigenfrequency $\Delta\Omega(\phi)$ in an anharmonic potential; indeed the Lydane-Sachs-Teller relations require $\Delta\varepsilon \propto -\Delta\Omega$ [27]. The changes in the losses (real part of the conductivity) are expected to be much smaller. Rutile exhibits incipient ferroelectric trends [28] accompanied by softening upon cooling of A_{2u} (172 cm^{-1} at room temperature) and E_u (189 cm^{-1} at room temperature) polar phonons [29]. It is then expected that the transient contribution to the permittivity of these two modes due to a lattice heating would be negative. Nevertheless, our experiments do not allow us to determine to which extent these or other phonon modes are involved in the carrier thermalization and cooling and what is their out-of-equilibrium contribution.

The observed contribution to the transient permittivity can be also ascribed to the polaronic character of mobile charge carriers in rutile. The slow itinerant polaron motion is characterized by the Drude-like response at THz frequencies as observed in our experiments. Internal degrees of freedom of medium or large polarons, i.e., the hydrogenlike spectrum reflecting the quasiparticle excitation or ionization, appear in the mid- or near-infrared spectral range [30] and contribute to the polarization in the THz region.

Recently, an absorption peak in rutile has been observed at 115 meV and assigned to the intrinsic absorption in polaron trap states [31]. Using DFT calculations, these authors determined the ionization energy and the Bohr radius of the hydrogenlike potential in which the electron moves ($E_{\text{ion}} = 0.38$ eV, $a_B \approx 4$–5 Å). For an order-of-magnitude estimation of the strength of the polaron ionization response at THz frequencies, we consider only the lowest ($1s \rightarrow 2p$) hydrogenlike transition, which provides the dominant contribution to the permittivity. The corresponding polaronic dielectric strength is calculated using the Fermi's golden rule:

$$\varepsilon_{\text{pol}}(\omega) = \frac{1}{\varepsilon_0}\frac{4Ne^2}{E_{2p} - E_{1s} - \hbar\omega - i\gamma}|\langle 1s|z|2p\rangle|^2$$

$$\approx \frac{\alpha\phi e^2}{\varepsilon_0 E_{\text{ion}}}2.2a_B^2. \qquad (13)$$

The order-of-magnitude estimate for the lowest excitation fluence (2×10^{17} photons/cm^2) from this formula is $\varepsilon_{\mathrm{pol}} \approx 0.4$; this contribution is added to the background permittivity of the material $\varepsilon_{\mathrm{bkg}}$ formally defined as a low-frequency permittivity with the polaronic effect subtracted ($\varepsilon_{\mathrm{bkg}} \approx 90$, cf. Fig. 1). Following (13), an increase of the photon excitation fluence ϕ leads to an increase of $\varepsilon_{\mathrm{pol}}$. However, at high carrier densities, this increase of the material permittivity induces a polaron softening (decrease of the ionization energy and of the energy of polaronic transitions) and an increase of its transition dipole moment. Indeed, in the hydrogen-atom model, the energies of the intrapolaronic transitions are inversely proportional to the square of the surrounding permittivity: $E_{\mathrm{ion}} \propto (\varepsilon_{\mathrm{bkg}} + \varepsilon_{\mathrm{pol}})^{-2}$, and the Bohr radius scales with this permittivity: $a_B \propto (\varepsilon_{\mathrm{bkg}} + \varepsilon_{\mathrm{pol}})$. In other words, polarons "feel" each other through their contribution to the permittivity of the lattice. Equation (13) then represents a nonlinear equation for $\varepsilon_{\mathrm{pol}}$ due to the polaron-polaron interaction and the effect of the high carrier density can become very significant. For example, solution of this nonlinear equation yields $\varepsilon_{\mathrm{pol}} \approx 20$ at the excitation fluence of 5×10^{18} photons/cm^2. This is, of course, a very crude reasoning; however, it shows that the sign and the order of magnitude of the expected effect is the one that we have experimentally observed.

Based on the current experimental results we are unable to draw more quantitative conclusions. It would be extremely useful to perform a similar pump-probe study using a probing pulse in the multi-THz frequency range, where the transient contributions of the phonon modes and of the polarons can be directly spectrally resolved and the origin of the transient permittivity could be assigned.

V. CONCLUSION

Charge transport in (001)-oriented rutile was investigated in detail using time-resolved THz spectroscopy at temperatures between 10 and 300 K. Photoexcitation by femtosecond pulses at 266 nm gives rise to a highly inhomogeneous carrier density in the vicinity of the surface. The data can be fitted with a simple Drude response at low excitation fluences (both at low and at high temperatures). However, experiments at higher fluences reveal a very complex underlying behavior.

At low temperatures this stems from the fact that electron-hole scattering strongly influences the carrier mobility close to the photoexcited surface. Moreover, the carrier concentration close to the surface decreases on a tens of picosecond time scale due to ambipolar diffusion of carriers towards the bulk of the crystal and, in turn, the average carrier mobility increases.

We developed a general plasma diffusion model relating all these phenomena to the evolution of measured transient THz conductivity during the first nanosecond. This allowed us to quantify the carrier scattering, recombination, and ambipolar diffusion at low temperatures, and to assess the role of the electron-hole scattering and of the mobility of electrons and holes in the charge transport.

Finally, at room temperature a competition between the polaron itinerant Drude-like motion, hot phonon contribution, and polaron internal degrees of freedom is observed. The measured transient modulation of the permittivity due to the nonequilibrium phonon and polaron population is very strong (up to $\Delta\varepsilon = 50$). Optical pump–multi-THz probe experiments may be very useful to elucidate which phonon modes contribute the most to the transient permittivity and whether the polaronic ionization effect plays an important role in this interaction. The motivation is even stronger if we consider the incipient ferroelectric character of TiO$_2$ and that our results show the possibility to observe the tuning of the dielectric constant by means of optical excitation and carrier-phonon coupling.

[1] R. G. Breckenridge and W. R. Hosler, Phys. Rev. **91**, 793 (1953).

[2] M. Grätzel, Nature **414**, 338 (2001).

[3] E. Hendry, F. Wang, J. Shan, T. F. Heinz, and M. Bonn, Phys. Rev. B **69**, 081101(R) (2004).

[4] E. Hendry, M. Koeberg, J. Pijpers, and M. Bonn, Phys. Rev. B **75**, 233202 (2007).

[5] S. A. Jensen, K.-J. Tielrooij, E. Hendry, M. Bonn, I. Rychetský, and H. Němec, J. Phys. Chem. C **118**, 1191 (2014).

[6] E. Hendry, M. Koeberg, B. O'Regan, and M. Bonn, Nano Lett. **6**, 755 (2006)

[7] H. Němec, V. Zajac, I. Rychetský, D. Fattakhova-Rohlfing, B. Mandlmeier, T. Bein, Z. Mics, and P. Kužel, IEEE Trans. Terahertz Sci. Technol. **3**, 302 (2013).

[8] P. Tiwana, P. Parkinson, M. B. Johnston, H. J. Snaith, and L. M. Herz, J. Phys. Chem. C **114**, 1365 (2010).

[9] P. Kužel and H. Němec, J. Phys. D: Appl. Phys. **47**, 374005 (2014).

[10] M. Cardona and G. Harbeke, Phys. Rev. **137**, A1467 (1965).

[11] C. Jacoboni, *Theory of Electron Transport in Semiconductors* (Springer, Berlin, 2010).

[12] H. Němec, L. Fekete, F. Kadlec, P. Kužel, M. Martin, J. Mangeney, J. C. Delagnes, and P. Mounaix, Phys. Rev. B **78**, 235206 (2008).

[13] L. Fekete, H. Němec, Z. Mics, F. Kadlec, P. Kužel, V. Novák, J. Lorinčík, M. Martin, J. Mangeney, J. C. Delagnes, and P. Mounaix, J. Appl. Phys. **111**, 093721 (2012).

[14] V. Zajac, H. Němec, C. Kadlec, K. Kůsová, I. Pelant, and P. Kužel, New J. Phys. **16**, 093013 (2014).

[15] L. Fekete, P. Kužel, H. Němec, F. Kadlec, A. Dejneka, J. Stuchlík, and A. Fejfar, Phys. Rev. B **79**, 115306 (2009).

[16] W. G. Spitzer, R. C. Miller, D. A. Kleinman, and L. E. Howarth, Phys. Rev. **126**, 1710 (1962).

[17] See Supplemental Material at http://link.aps.org/supplemental/10.1103/PhysRevB.94.115206 for details on the two-component Drude model and for a more technical discussion of the experimental spectra fitting.

[18] J. Yahia, Phys. Rev. **130**, 1711 (1963).

[19] D. S. Boudreaux, F. Williams, and A. J. Nozik, J. Appl. Phys. **51**, 2158 (1980).

[20] J. J. Kasinski, L. A. Gomez-Jahn, K. J. Faran, S. M. Gracewski, and R. J. Dwayne Miller, J. Chem. Phys. **90**, 1253 (1989).

[21] C. Kormann, D. W. Bahnemann, and M. R. Hoffmann, J. Phys. Chem. **92**, 5196 (1988)

[22] B. Enright and D. Fitzmaurice, J. Phys. Chem. **100**, 1027 (1996).

[23] C. Persson and A. Ferreira da Silva, Appl. Phys. Lett. **86**, 231912 (2005).

[24] M. Dou and C. Persson, J. Appl. Phys. **113**, 083703 (2013).

[25] K. M. Glassford and J. R. Chelikowsky, Phys. Rev. B **46**, 1284 (1992).

[26] A. Pashkin, M. Porer, M. Beyer, K. W. Kim, A. Dubroka, C. Bernhard, X. Yao, Y. Dagan, R. Hackl, A. Erb, J. Demsar, R. Huber, and A. Leitenstorfer, Phys. Rev. Lett. **105**, 067001 (2010).

[27] A. S. Barker, Jr., Phys. Rev. B **12**, 4071 (1975).

[28] A. Grünebohm, P. Entel, and C. Ederer, Phys. Rev. B **87**, 054110 (2013).

[29] F. Gervais and B. Piriou, Phys. Rev. B **10**, 1642 (1974).

[30] D. Emin, Phys. Rev. B **48**, 13691 (1993).

[31] H. Sezen, M. Buchholz, A. Nefedov, C. Natzeck, S. Heissler, C. Di Valentin, and C. Wöll, Sci. Rep. **4**, 3808 (2014).